Sustainable Materials and Technologies 38 (2023) e00767

Contents lists available at ScienceDirect

Sustainable Materials and Technologies

journal homepage: www.elsevier.com/locate/susmat

Recycling of glass waste and spent alkaline batteries cathodes into insulation materials

Luca Cozzarini *, Lorenzo De Lorenzi, Lorenzo Fortuna, Paolo Bevilacqua

University of Trieste, Department of Engineering and Architecture, Via Valerio 6/A, I-34127 Trieste, Italy

ARTICLE INFO

Keywords:
Expanded glass
Glass recycling
Alkaline battery recycling
Thermal insulating materials
Soundproofing materials
Circular economy
Mechanical test
X-ray microtomography

ABSTRACT

Expanded glass with thermal and acoustic insulation properties are obtained from a foaming blend composed of 97% glass waste and 3% expanding agent. This latter is a blend of carbon and manganese oxides, recovered from exhausted alkaline batteries. The samples are produced after heating the mixture in a ventilated furnace at temperatures between 850 and 950 °C, for times between 15 and 60 min. Mechanical, thermal and acoustic properties are characterized as a function of process parameters. The glass foam samples have densities in the range of 290–350 kg/m^3, porosity of 86–90%, thermal conductivity values of 107–120 mW m^{-1} K^{-1}, noise reducing factors of 0.2–0.3 and compressive strengths up to 4.6 MPa. Although the resulting insulating performances are not as outstanding as those of polymer foams or mineral wool, these materials can emerge as competitive candidates for applications requiring low weight and moderate thermal and acoustic insulation properties, in combination with non-flammability and high temperature load bearing-capacity. Moreover, the use of 100% recycled raw materials limits the energy and the resource required for their production, if compared to those needed for the extraction, transportation, and processing of primary raw materials, making these foams attractive also in terms of environmental impact.

1. Introduction

The demand for insulation materials has seen a significant increase in recent years, driven by the growing emphasis on energy efficiency and sustainable building practices. This upward trend is expected to continue as stricter energy efficiency regulations and incentives for sustainable building practices are implemented worldwide [1–3]. Heating, ventilation, and air conditioning of enclosed spaces currently account for roughly 40% of energy consumption and carbon emissions [4–6]. Therefore, enhancing energy efficiency and ensuring adequate insulation in buildings are of paramount importance to reduce energy consumption and emissions associated with the burning of fossil fuels [7,8]. Nowadays, the insulation materials market is dominated by organic foams like expanded polystyrene (EPS) or foamed polyurethane (PU), as well as inorganic fibrous materials like glass or mineral wool (GW, MW) [7,9,10]. Each material has its own advantages and disadvantages, and the selection depends on various factors, such as the specific application, location, climate, and budget. Traditional insulators are primarily produced from primary raw sources, such as fossil fuels or minerals. However, the use of secondary and renewable raw materials has become crucial in meeting ecological and sustainability requirements, leading to a growing investigation for insulating materials produced from natural or recycled sources [7,11–14]. Some studies have demonstrated the feasibility utilizing bio-based or natural raw sources [15–19], while others have focused on recycling plastics or textile fibers into insulation panels. Other work has focused specifically on producing foams from recycled glass [20–24].

A promising solution to recycle glass into an insulation material is the production of expanded glass: typically, a fine glass powder is mixed with a foaming compound and other additives; the mixture is subsequently heated above the softening point of the glass; the gas released from the foaming agent expands in the viscous mass, increasing the volume of the sample and leading to a porous structure [25–27]. After cooling at room temperature, the porous structure is preserved, resulting in a lightweight, rigid material [28–30]. Glass foams are lightweight (density 100–300 kg m^{-3}) while retaining adequate mechanical strength. Moreover, they are inert, chemically stable, not flammable and immune to biological degradation [31,32]. Common foaming agents are carbonates, such as calcium, sodium and magnesium carbonate ($CaCO_3$, Na_2CO_3 and $MgCO_3$). They thermally decompose into calcium, sodium

* Corresponding author.
E-mail address: lcozzarini@units.it (L. Cozzarini).

https://doi.org/10.1016/j.susmat.2023.e00767
Received 28 July 2023; Received in revised form 16 October 2023; Accepted 2 November 2023
Available online 4 November 2023

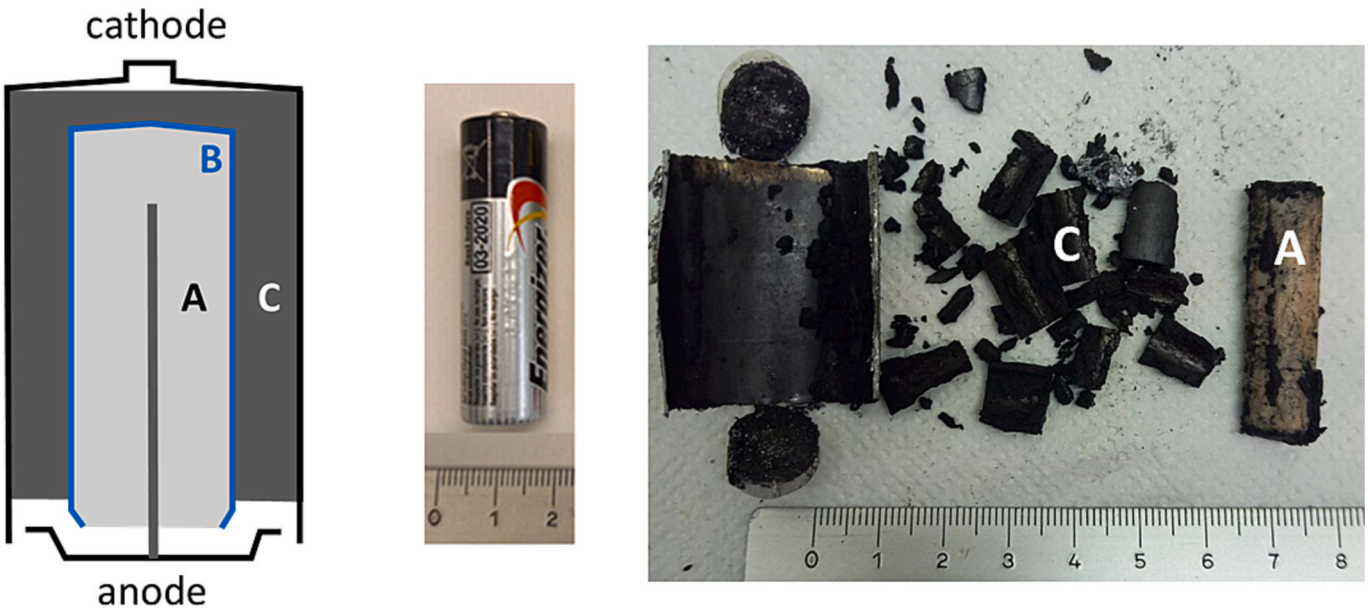

Fig. 1. From left to right: schematics of an alkaline battery; typical alkaline battery before and after cutting. "A" denotes the anodic inner cylinde (composed of Zn and KOH); "B" the porous separator; "C" the cathodic outer cylinder (composed of Mn oxides and graphite).

and magnesium oxides (CaO, Na_2O and MgO), releasing carbon dioxide (CO_2), which is responsible for the glass foaming [26]. Nonetheless, since these oxides are also major constituents of many silica glass formulations, the change in their ratios inside the glass can modify its viscosity and final characteristics. Carbon-based foaming agents, such as organic compounds, release CO_2 upon oxidation while leaving no solid residues that modifies glass properties [29,31]. Organic molecules tend to undergo rapid oxidation in the presence of air at high temperatures (800–900 °C). However, in the case of the foaming mixture, these compounds are primarily exposed to air only at the surface, since the molecules within the mixture are effectively insulated from the air by the softened glass. Consequently, these molecules are more likely to undergo pyrolysis and carbonization instead of oxidation. To address this issue, suitable oxidant reagents such as Mn or Fe oxides are used alongside organic compounds [29,33]. Mn oxides are preferred over Fe oxides, because these latter compounds act as networks modifiers by introducing non-bridging oxygen, thus increasing the softening point and the viscosity of the glass [34,35]. It has been shown that Mn IV oxide (MnO_2) act both as foaming agent and as oxidant, since it thermally decomposed at lower oxidation states releasing oxygen gas, which can contribute to foaming process while oxidizing the carbon molecules [29,36].

In our previous studies [37,38], we demonstrated the production and characterization of expanded glass produced from secondary sources, such as cullet recovered from municipal glass waste collection as the glass source, and textile waste as the carbon source. However, we also used primary Mn IV oxide purchased as a chemical reagent.

In this research work, we present and discuss the production of foamed glass using a similar protocol, but with a mixture of Mn oxides and graphite recovered from the cathodes of exhausted alkaline batteries as the foaming agent, which can represent an innovative approach compared to traditional reagent-grade Mn oxide. The foaming mixture consists solely of secondary raw materials, with 97% container glass waste and 3% exhausted alkaline battery cathodes. We will also examine how the mechanical and functional properties of the expanded glass differ when using recycled Mn oxides instead of pure primary Mn IV oxide. The performance of the glass foam produced from glass cullet and spent alkaline battery cathodes was found to be lower compared to the glass foam made with reagent-grade Mn oxide. The reduced performance can be attributed to variations in the chemical composition and purity of the waste materials.

Despite these limitations, the utilization of waste materials offers significant advantages in terms of environmental sustainability, waste valorization, and the circular economy. Furthermore, waste materials, including glass waste and spent alkaline battery, are abundant and often available at lower or no cost, enhancing the economic viability of the proposed method and making it feasible for large-scale implementation. The utilization of waste materials also leads to cost savings, further incentivizing the adoption of sustainable practices. In 2020, approximately 230,000 tons of alkaline batteries were sold in the EU [37]. An average portable alkaline battery (AA type) weighs around 23–24 g, with the cathode accounting for about 10 g (9 g of Mn oxides and 1 g of graphite) [39–41]. Considering the staggering amount of glass waste generated in the EU, with 17.9 million tons in 2020 and 15.2 million tons from glass packaging [42,43], the proposed method holds significant potential for scalability and replicability, contributing to the reduction of landfill waste and the need for virgin materials. This approach aligns with circular economy principles, promoting resource conservation, the transformation of waste materials into value-added products, and minimizing environmental impact while closing material loops and reducing reliance on finite resources.

The combination of insulation properties, thermal stability and mechanical properties allow the expanded glass to be considered for use in load bearing parts, which is typically not the case for other traditional insulating materials. Thanks to these characteristics, it can be evaluated as a valuable solution for thermal and acoustic insulation in many sectors, as it possess thermal, chemical and mechanical stability generally superior to that of polymer foams [32,44,45]. Its higher unit price and higher thermal conductivity with respect to polystyrene foam or mineral fibers [29,44] may be counterbalanced by environmental footprint and circular economy advantages outlined above.

2. Material and methods

2.1. Raw materials

Transparent glass was obtained after sorting container glass waste. The glass cullet was washed and then reduced to a granulate by jaw crushers and cylindrical mills (SAIMA). The resulting material was sieved to achieve a particle size ranging from 1.5 to 2.8 mm.

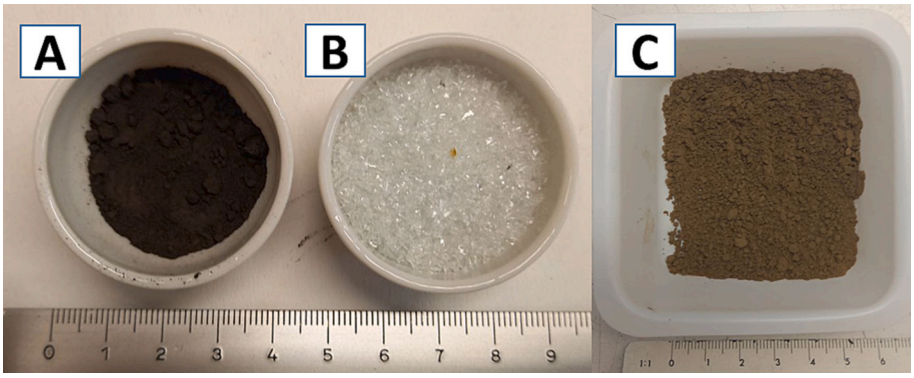

Fig. 2. Powder obtained from cathode (A), glass granulate (B) and final foaming mixture (C).

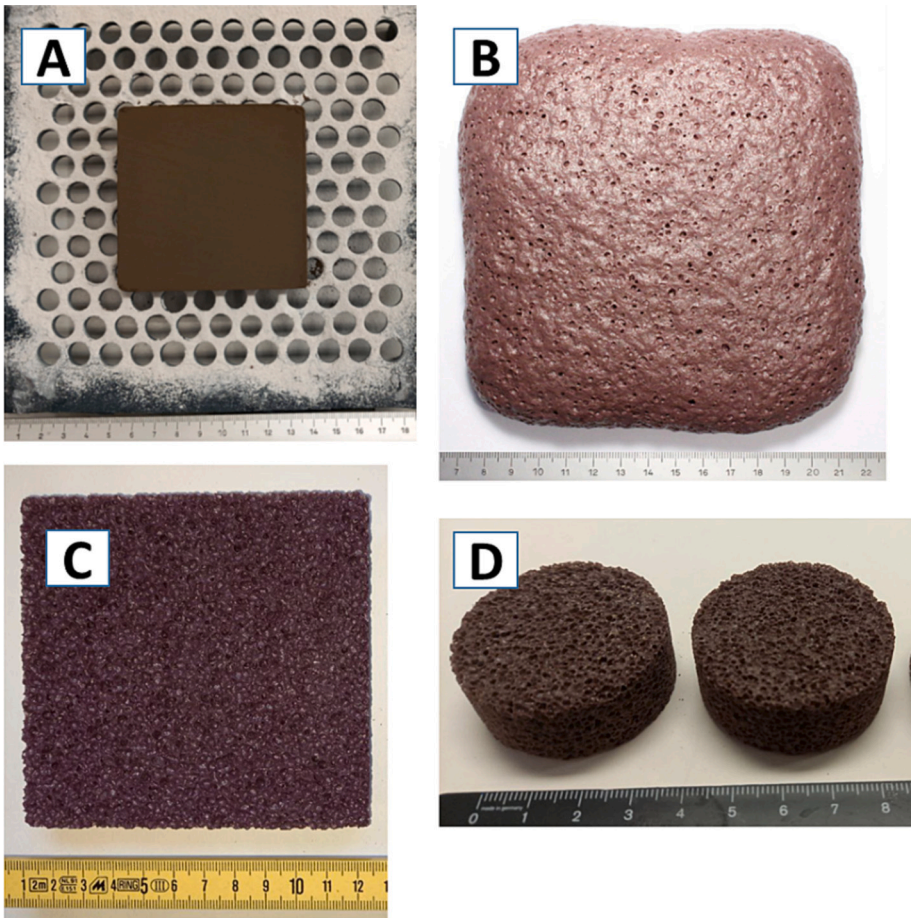

Fig. 3. Example pictures of: green sample before heat treatment (A); expanded sample after heat treatment (B); square-based cut sample (C) and cylindrical shape cut samples (D).

Exhausted alkaline batteries, sourced from various manufacturers, were obtained through separate collection of waste batteries. The average content of different components (cathode, anode, metal casing) was determined after cutting, opening and weighting 20 spent batteries from different manufacturers. Fig. 1 depicts a schematic representation of an alkaline battery, along with photos illustrating the batteries before and after opening. The batteries were cut lengthwise, and upon removing the metal casing, the dark-colored outer cylinder (cathode, containing manganese oxide powder and graphite, denoted as "C" in Fig. 1) was separated from the lighter-colored inner cylinder (a mixture of zinc and potassium hydroxide, denoted as "A" in Fig. 1). The dark powder obtained was dried at 80 °C for 24 h and subsequently finely ground.

The final foaming mixture was prepared by blending 97% glass granulate and 3% dried powder from the alkaline battery cathode (expressed as weight percentages). This mixture was pulverized using a Herzog mill for 70 s, resulting in a fine powder. Fig. 2 shows the glass granulate and the final foaming mixture.

2.2. Raw materials characterization

The density of glass powder was determined with a Gay-Lussac picnometer. Chemical analysis of glass was performed by X-Ray Fluorescence (Olympus Vanta C Series, VCA) with a 4 W Ag anode X-ray

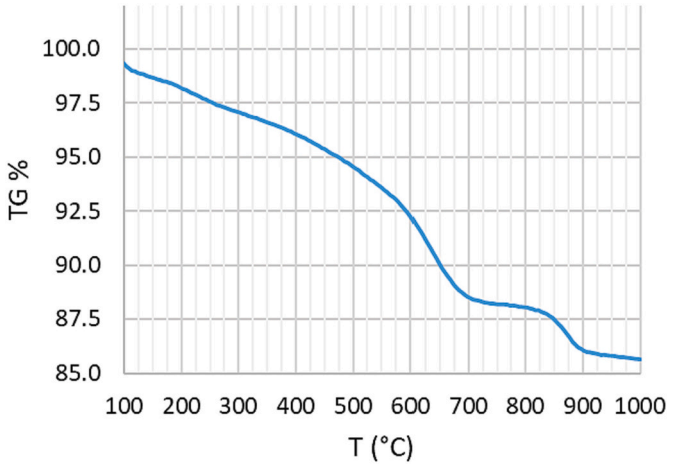

Fig. 4. TG curve of cathode mix heated in air.

tube, silicon drift detector (SDD) and an excitation source ranging from 8 to 50 keV; results were quantified using certified oxide standards.

Thermogravimetry (TG) of the cathode powders and the foaming mixture was performed using a Netzsch STA 409EP with alumina crucibles, from 20 °C to 1000 °C, with heating rate of 10 °C·min^{-1}. XRD patterns were recorded on a Bruker D5005 diffractometer, using Cu Kα (E = 8.04 keV; λ = 1.5406 Å), operating at 40 kV-20 mA over a 10° < 2θ < 70° angular range (angular resolution: 0.05°; time/step: 5 s).

The thermal behavior of the glass was analyzed using a hot stage microscope (HSM, Misura, Expert System Solutions, Modena, Italy). The glass powders were compacted by uniaxial pressing into small cylinders (diameter: 1 mm, height: 3 mm) and heat-treated from 20 to 1250 °C at a rate of 10 K min^{-1}. The system software (Misura™4, Expert System Solutions, Modena, Italy) automatically analyzed the acquired sample images during the test. Based on geometric parameters derived from the shape of the test piece (height, width, contact angle), the software determined the characteristic temperatures (sintering, softening, sphere, and hemisphere) according to international standards such as DIN 51730, ASTM D1857, and ISO 540. Similarly, the expansion behavior of the foaming mixture was determined by monitoring the evolution of the area of the acquired images (A) respect to the initial area (A_0) as a function of temperature. The collected data were useful to determine the optimal process window for the foam production and discuss the results regarding mechanical and functional properties.

2.3. Foam production

The procedure is described in details in a previous work of ours [37]. In summary, 125 g of the foaming mixture were inserted in a square steel mold (8 × 8 cm^2); the mixture was first leveled manually (slight compression with the top of the mold) and then pressed by applying 255 kN load for three minutes with a Weber PW40 hydraulic press. This resulted in a green of 8 × 8 × 1 cm^3 (Fig. 3 A). The green was heated in a FALC FM13 muffle with a heating ramp of 10 K min^{-1} up to at a predetermined temperature (from 850 °C to 925 °C); this temperature was hold for 15 to 60 min. After the specified time, the sample was quickly extracted from the furnace to undergo rapid cooling down to 550 °C - 600 °C. Subsequently, it was cooled slowly in hot air for 2–3 h until reaching room temperature inside the furnace turned off. Rapid cooling

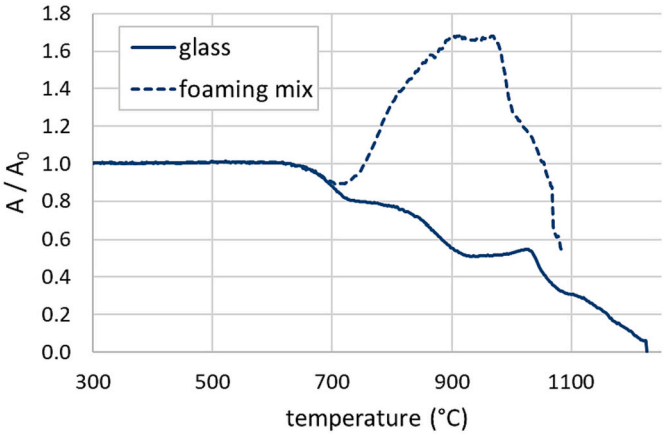

Fig. 6. HSM A/A_0 value as a function of temperature for glass (continuos line) and foaming mixture (dashed line).

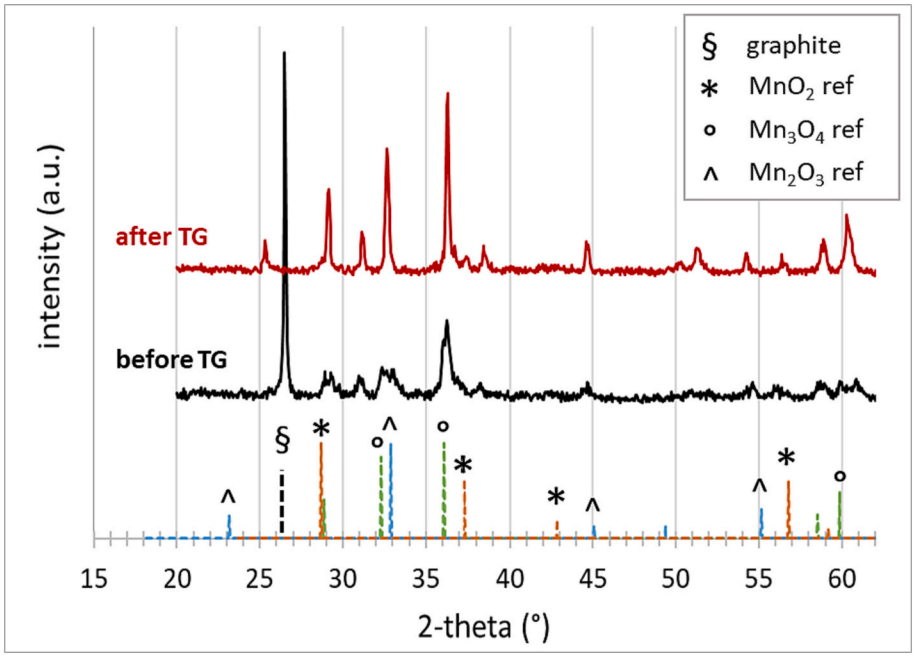

Fig. 5. XRD diffractograms of cathode mixture before TG (black curve) and after TG (red curve).

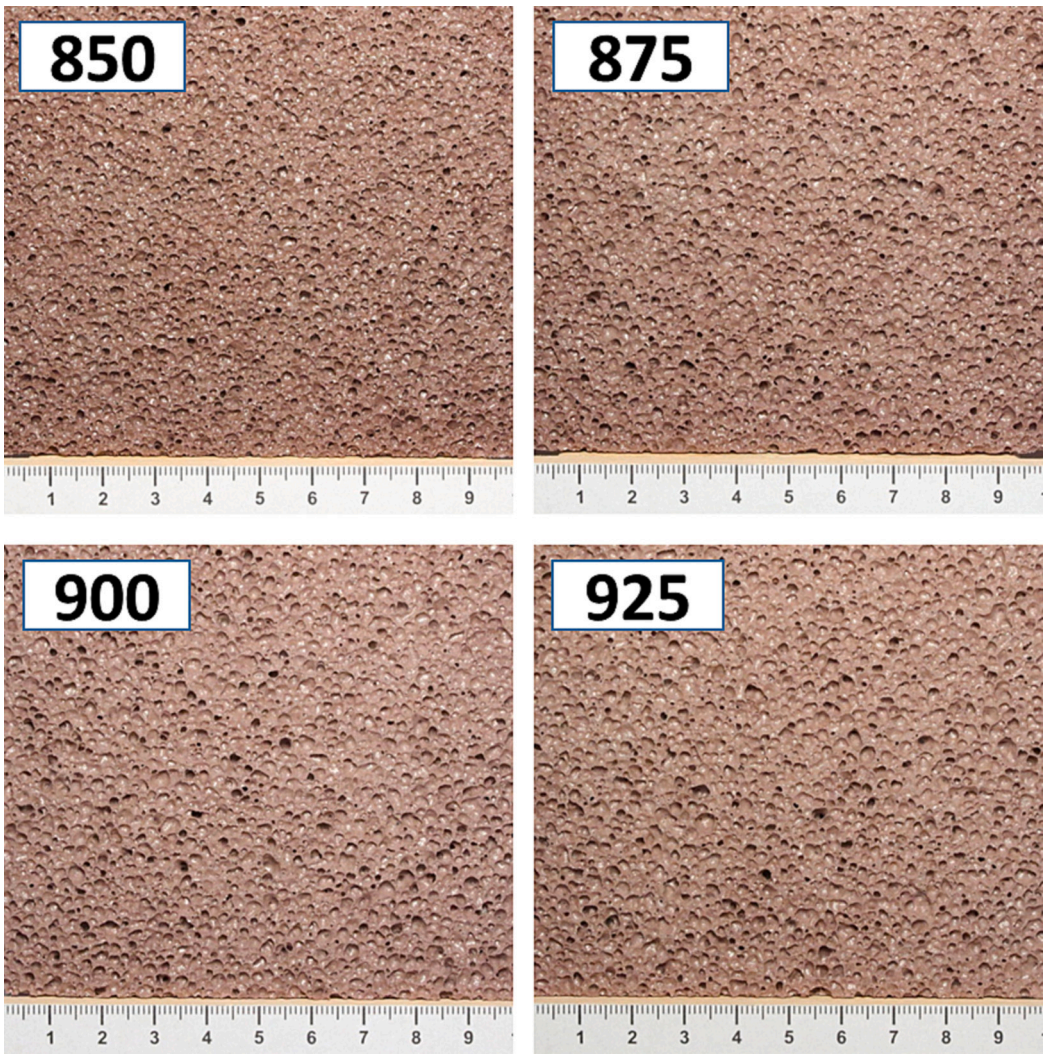

Fig. 7. Representative pictures of the expanded glass obtained at 850 °C, 875 °C, 900 °C and 925 °C for sintering time of 15 min.

was necessary to solidify the expanded structure and increase the glass viscosity abruptly, while the subsequent slow cooling prevented specimen breakage due to thermal contraction stresses. The samples were named according to the process temperature. For example, a sample named "850" corresponds to a sample sintered at 850 °C. For comparison, other samples were prepared at the same temperature and times with a foaming mixture obtained by blending 96.5% glass granulate, 1% dried textile waste powder and 2.5% MnO_2 (as previously reported in a work of ours).

2.4. Samples dimension, mass and density

Sintered samples (average dimension: about 15 × 15 × 2.5 cm^3, as seen in Fig. 3 B) were cut into regular geometrical shapes (square-based or cylindrical, as seen in Fig. 3 C and D). The dimensions were measured with a digital caliper (RS pro, code 841–25), rounding the value to 10^{-1} mm (average of three measurements for each dimension). The mass was determined with a digital balance (Sartorius CP244S), rounding the value to 10^{-1} g, while the volume was calculated as the product of the three dimensions (in the case of square-based samples), or according to $\pi R^2 H$ (with R radius and H height) for cylindrical samples. The density of the samples (rounded value to kg m^{-3}) was calculated by dividing the mass by the volume.

2.5. Porosity characterization

A volume of 15x15x15 mm^3 was cut from the center of each representative sample and characterized by X-ray microcomputed tomography (μCT). Acquisitions were performed by means of a custom-made cone-beam system (TOMOLAB, Elettra-Sincrotrone Trieste), with a resolution of 8 μm, beam energy of 40 kV and intensity 200 μA, and an exposure time of 2.5 s. Three-dimensional slices were reconstructed and processed with FIJI package of ImageJ2 software.

2.6. Mechanical tests

Compression tests were performed using a Shimadzu AGS-X 10 dynamometer (10 kN load cell). The test speed was set to 1.5 mm min^{-1}, while the signal acquisition time was set at 0.25 s. Mechanical properties (compression modulus E and compression strength σ_M) were determined according to ASTM C165, procedure "A" [46]. Compression toughness was determined as the area under the stress-strain curve. Five samples were tested for each process condition.

2.7. Sound absorption properties

A two-microphone plane wave impedance tube (Kundt's tube) was used to determine the sound absorption properties of samples, according to the ISO 10534-2 standard [47]. Three cylindrical samples (diameter:

Table 1
Sample properties: density (ρ), thermal conductivity (λ), compression modulus (E_C), compression strenght (σ_C) and compression energy (K). Values of samples obtained using reagent grade MnO_2 are reported for comparison.

Sample	ρ (kg m^{-3})	λ (mW m^{-1} K^{-1})	NRC	E_C (MPa)	σ_C (MPa)	K (J)
850.15	327 ± 5	116 ± 1	0.20	57.5 ± 10.1	1.9 ± 0.5	6.9 ± 0.3
862.15	318 ± 4	109 ± 1	0.20	58.8 ± 1.7	2.1 ± 0.4	7.3 ± 0.8
875.15	309 ± 4	111 ± 1	0.20	61.8 ± 4.3	2.7 ± 0.2	9.4 ± 0.7
888.15	296 ± 3	108 ± 2	0.20	61.3 ± 11.5	2.5 ± 0.3	11.4 ± 2.1
900.15	293 ± 4	107 ± 2	0.20	60.7 ± 8.9	2.8 ± 0.2	11.6 ± 0.9
925.15	285 ± 2	106 ± 3	0.20	70.5 ± 12.6	2.7 ± 0.3	16.2 ± 3.1
950.15	292 ± 3	107 ± 3	0.20	83.5 ± 4.6	3.0 ± 0.1	18.3 ± 0.5
850.30	341 ± 3	114 ± 2	0.25	73.2 ± 10.6	3.0 ± 0.5	11.3 ± 2.4
850.60	353 ± 4	120 ± 3	0.20	79.9 ± 4.8	4.6 ± 0.4	12.9 ± 0.5
925.30	286 ± 5	108 ± 3	0.25	74.9 ± 4.1	3.0 ± 0.2	15.1 ± 1.9
925.60	290 ± 5	109 ± 1	0.30	76.5 ± 1.4	3.0 ± 0.1	14.2 ± 1.3
(MnO_2) 850.45	190 ± 2	79 ± 1	0.40	53.6 ± 3.1	1.5 ± 0.1	14.5 ± 0.4
(MnO_2) 875.45	181 ± 4	83 ± 2	0.40	63.6 ± 8.6	1.1 ± 0.1	8.8 ± 1.6
(MnO_2) 900.45	178 ± 4	85 ± 2	0.40	58.6 ± 6.6	0.9 ± 0.1	3.9 ± 1.2

44 mm; thickness: 18 mm) were tested for each process condition.

2.8. Thermal conductivity measurements

The thermal conductivity was measured with a Netzsch HFM 446 heat flow meter on square-based samples (100 × 100 × 18 mm^3) according to the technical standard ASTM C518 [48], at an average temperature of 25 °C. Three samples were tested for each sintering condition.

3. Results and discussion

3.1. Characterization of raw materials

The chemical analysis of glass powder is presented in Table S1 of the supplementary material, while the grain size distribution curves and characteristic diameters of the foaming mixture powder are displayed in Fig. S1 and Table S2 of the supplementary material. The particle sizes D_{50} and D_{90} of the mixture range from 16 to 17 μm and 88 to 90 μm, respectively. Table S3 of the supplementary material provides the average content of different components (cathode, anode, metal casing) in alkaline batteries. These data are consistent with the findings reported in the literature [39–41]. Notably, the cathode constitutes approximately half of the total battery weight, while the anode accounts for around 20% of the total battery weight. Fig. 4 illustrates the TG curves of the cathode mixture, and Fig. 5 presents the XRD patterns of the battery cathode mixture before and after TG. The diffraction pattern obtained prior to TG exhibits characteristic peaks corresponding to graphite and mixed manganese oxides. Following the heat treatment, the graphite diffraction peak disappears, and the relative intensity of the peaks

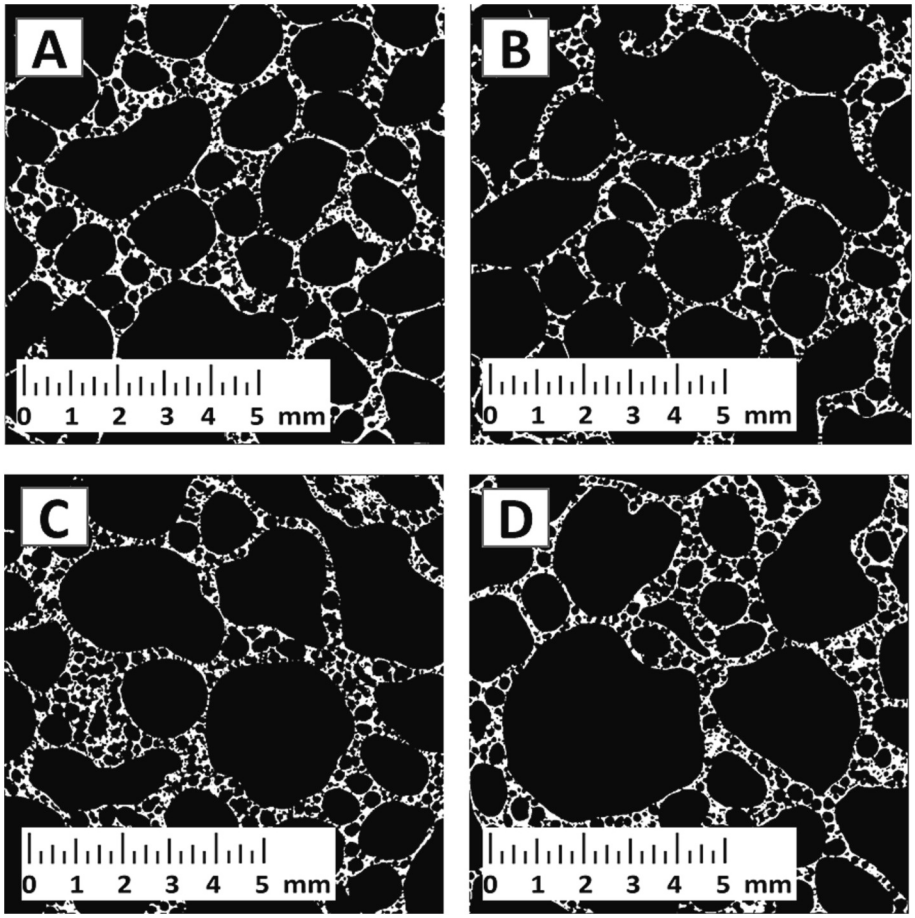

Fig. 8. Representative slices from micro-CT from the samples obtained at at 850 °C, 875 °C, 900 °C and 925 °C for sintering time of 15 min.

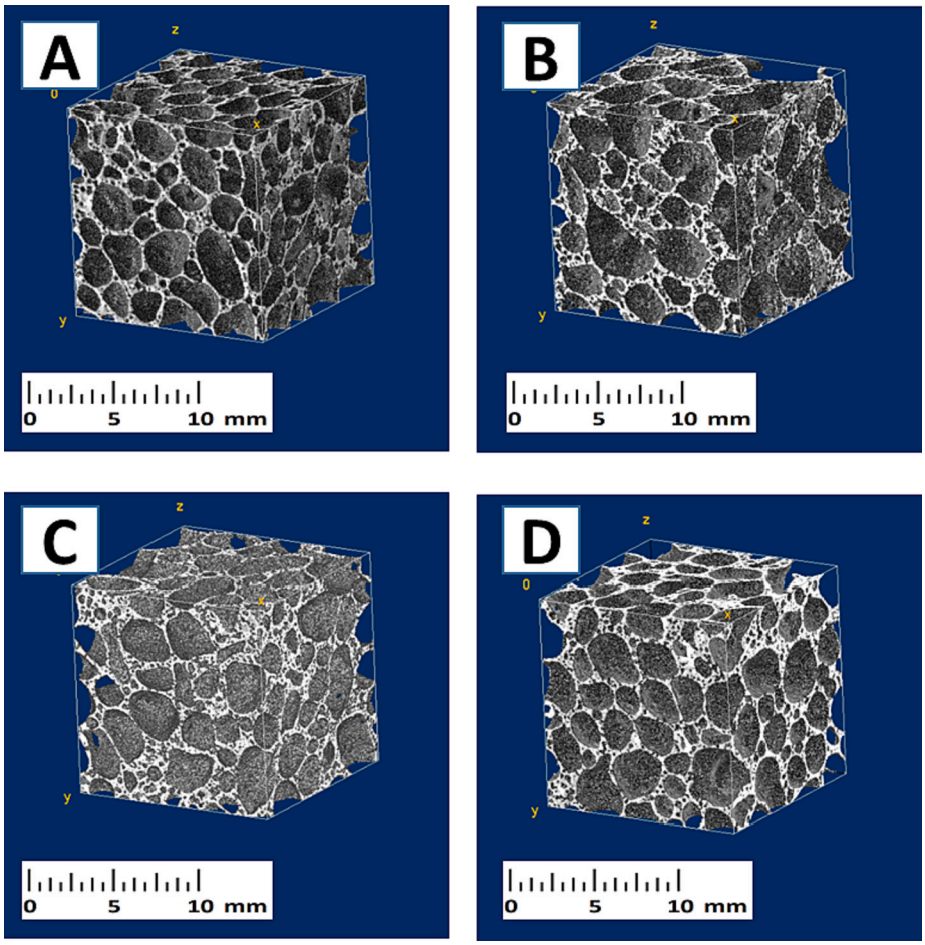

Fig. 9. Representative 3D volumes reconstructed from micro-CT data: sample prepared at 850 °C (A); 875 °C (B); 900 °C (C); 925 °C (D) for sintering time of 15 min.

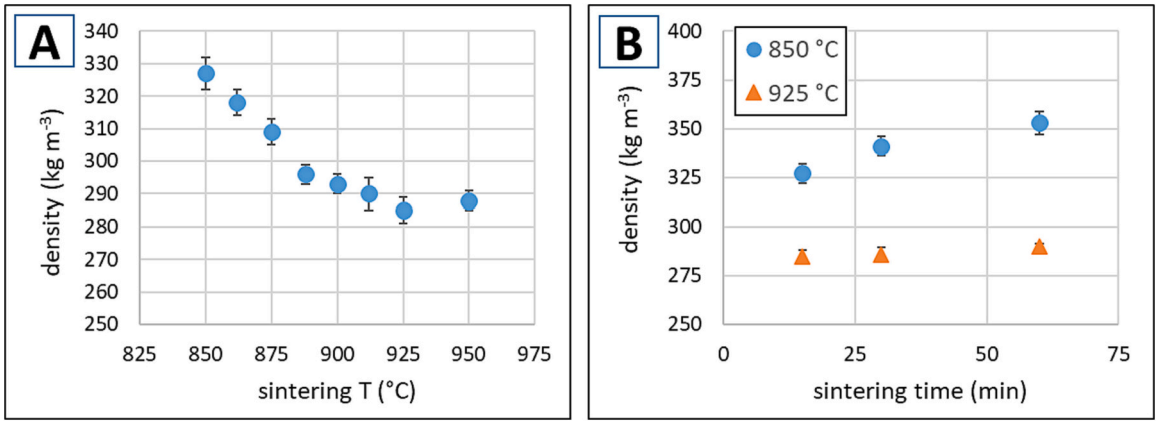

Fig. 10. Density of samples as a function of process temperature, for samples foamed for 15 min (A) and density of samples as a function of process time, for samples foamed at 850 °C and 925 °C.

associated with Mn II-III oxides increases compared to those associated with Mn IV oxide. Considering the weight loss of approximately 12% recorded by TG between room temperature and 750 °C (the first stage of weight loss) and the absence of the graphite-related peak in the diffractogram after TG, it can be attributed to the oxidation of graphite to CO_2. The second step of weight loss (approximately 2%) in the TG curve is likely associated with the decomposition of Mn IV oxide to Mn II-III oxide [36]. Therefore, we can estimate that the initial weight composition of the cathode mixture is approximately 88% mixed Mn oxides and 12% graphite. This finding aligns with the average composition of an alkaline battery cathode (approximately 11% graphite and 89% Mn oxide by weight) [39,40], as well as the data collected from an average of 20 alkaline batteries from different manufacturers (reported in Table S3 of the supplementary material).

3.2. *Monitoring of sample expansion*

The combination of a carbon-based foaming agent and an oxidant

Table 2
Cell wall thickness, pore size and % of porosity determined by micro-CT.

Sample	wall thickness (μm)	primary pore size (μm)	secondary pore size (μm)	porosity %
850.15	60 ± 9	1127 ± 94	225 ± 21	89.0
875.15	58 ± 9	1304 ± 107	216 ± 20	89.4
900.15	58 ± 9	1309 ± 108	223 ± 20	89.0
925.15	58 ± 9	1511 ± 132	215 ± 18	88.9
850.30	62 ± 9	1239 ± 103	236 ± 25	87.3
850.60	66 ± 10	1265 ± 150	238 ± 25	86.1
925.30	60 ± 9	1565 ± 114	227 ± 23	88.4
925.60 (MnO_2)	62 ± 9	1582 ± 150	219 ± 23	87.6
850.45 (MnO_2)	76 ± 23	1127 ± 94	225 ± 21	96.0
875.45	67 ± 21	1304 ± 107	216 ± 20	92.2

reagent has been already demonstrated as an effective method for producing low-density foamed glass [29,33,49,50]. Previous research has shown that MnO_2 act both as foaming agent and as oxidant, since it thermally decomposes at lower oxidation states releasing oxygen gas, which can contribute to foaming process and also oxidize the carbon molecules [29,51]. The carbon molecules react with oxygen, releasing CO_2 gas, which acts as a foaming agent. This gas production leads to the formation of pores within the softened glass mixture, resulting in a porous structure. The decomposition of MnO_2 happens in two stages: first, around 600 °C, it reduces to Mn III oxide (Mn_2O_3); then, around 850–900 °C, it further reduces to Mn II-III oxide (Mn_3O_4) [36]. In our study, we utilized a mixed Mn oxides derived from alkaline battery cathodes instead of chemically pure Mn IV oxide; the TG curve presented in Fig. 4 show the reduction steps discussed above. Following disappearance of the graphite diffraction peak in Fig. 5, It is also clear that the oxidation of carbon in the foaming mixture occurs effectively, causing an expansion of the samples. Density and type of porosity are directly determined by the viscosity, rate of bubble formation, and bubble coalescence [25,52]. Different studies reported that the optimal foaming point should be within the range where the foaming agent is active and the glass phase has a viscosity between 10^6 and 10^4 Pa • s (between the softening point and the flow point) [31,52]. These characteristic points can be determined experimentally by analyzing the hot-stage microscopy (HSM) data and tracking the evolution of the A/A_0 value, which represents the area evolution of the acquired HSM images relative to the original area of the cylinder. Monitoring the A/A_0 value as a function of temperature or time has proven to be a valuable method for highlighting important changes in the sample. A decrease in the value indicates sample shrinkage, while an increase is associated with expansion. Fig. 6 presents the evolution of the A/A_0 as a function of temperature for the glass (continuous line) and the foaming mixture (i.e., glass + expanding agent, dashed line).

Several shrinkage steps are observed for the glass: a first step just below 700 °C (sintering onset), a second step (softening) between 850 °C and 900 °C, and a sudden increase above 950 °C. At 1200 °C, the glass is considered melted ($A/A_0 = 0$). The sintering temperature is identified by the HSM software as the temperature at which the sample reaches a dimensional variation corresponding to 5% compared to the first acquired image, which is considered 100% ($A/A_0 = 0.95$). This point corresponds to a viscosity of approximately 10^{10} Pa·s. At this temperature, grain sintering starts: the sample decreases in size, but its shape does not substantially change. At the softening point (viscosity of about 10^6 Pa·s), the sample begins to show plasticity: the shape of the sample undergoes substantial changes, such as rounding of the corners and smoothing of the upper part of the walls. At the "sphere" temperature (viscosity of about 10^4 Pa·s), the sample is almost fluid, but it still possesses surface tension to counteract gravity. When the sample reaches the "hemisphere" temperature (where the height of the sample is equal to half the width of the base), the glassy material collapses. If the height of the sample is reduced to less than one third of the base, it is assumed that the sample has reached the melting point [31,53].

For the foaming mixture, after the initial shrinkage (sintering, just below 700 °C), an increase in the A/A_0 value is observed between 700 °C and 900 °C. The maximum expansion value is reached between 916 °C and 976 °C, followed by a decrease (shrinkage) above 980 °C. Pictures of the characteristic points of the foaming mixtures are reported in Fig. S3 of the supplementary material.

3.3. Sample properties

Representative pictures of the samples are reported in Fig. 7. Densities, thermal conductivities, mechanical and acoustic properties are reported in Table 1. Upon visual inspection, the overall structure of the expanded glass samples appears as a porous material, with thin walls separating macroscopic pores. Representative slices of samples from μ-CT scans are shown in Fig. 8; Fig. 9 shows two representative 3D reconstructed volumes from μ-CT analysis (additional macrographs,

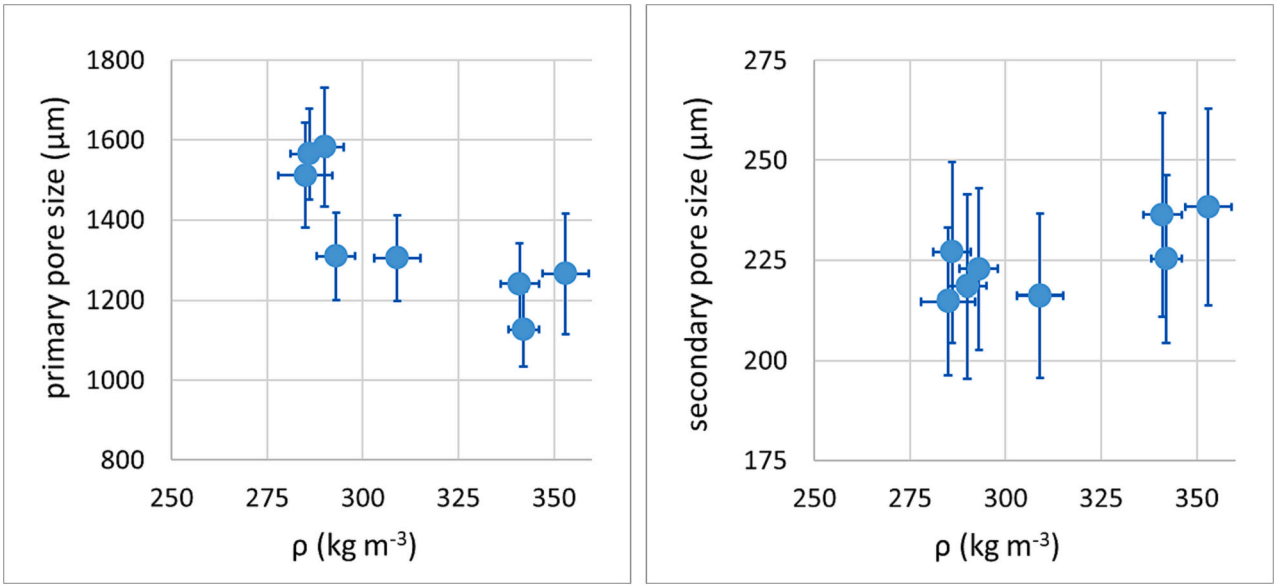

Fig. 11. Primary and secondary pore size as a function of glass foam density.

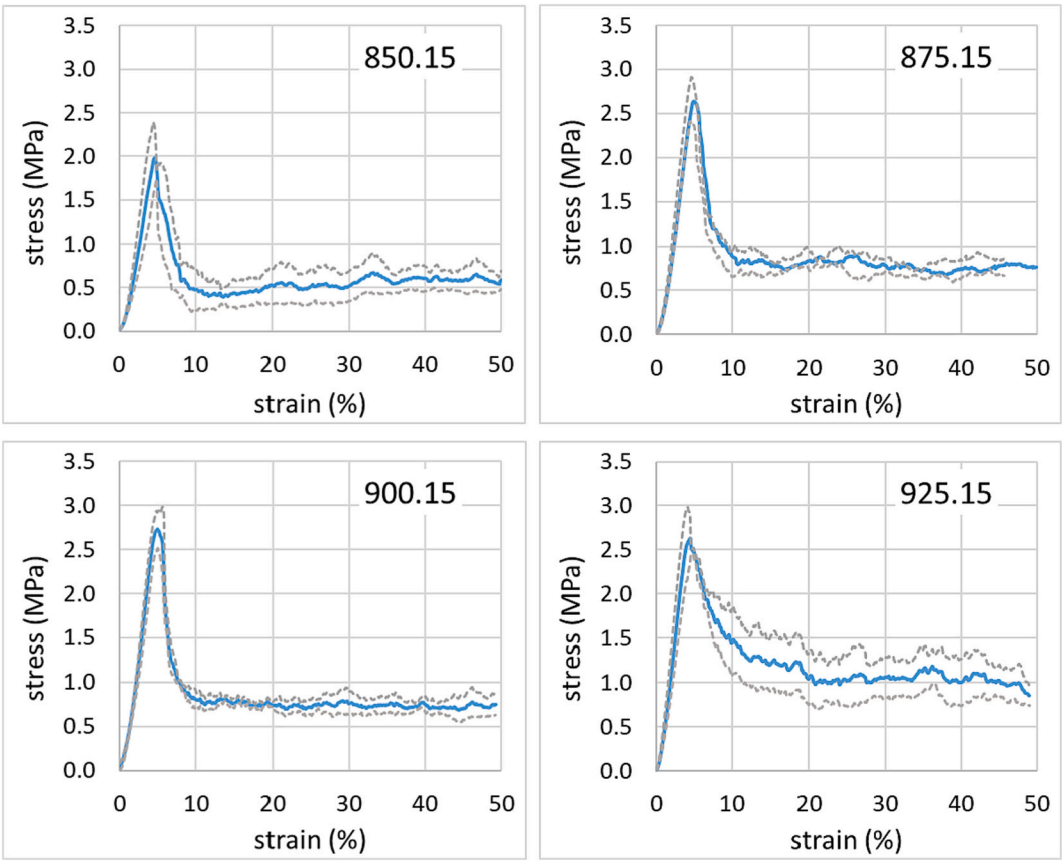

Fig. 12. Average compression stress-strain curves (in blue) of samples foamed for 15 min at different temperatures (850, 875, 900 and 925 °C). Dashed curves represent standard deviation (5 compression tests for each sample type).

micrographs, and 3D volume models of all the samples are available upon request). The images reveal the presence of primary macro porosity, ranging in the size of millimeters, as well as smaller secondary pores (ranging from 10 to 10^2 μm) within the cell walls.

3.4. Density

The density of the samples ranges from 285 to 333 kg m^{-3}. In comparison, typical mineral wools are lighter (100–150 kg m^{-3}) than our samples, while polymeric foams are even lighter (15–20 kg m^{-3}) [12,13,54,55]. Increasing foaming temperatures seem to lower density values (as noticeable in Fig. 10 A), while increasing foaming time seem to increase density value, especially for sample processed at 850 °C (as noticeable in Fig. 10 B). The lowest density is achieved for samples foamed at 925 °C for 15 min. Analyzing the porosity values (refer to paragraph 3.5), it can be deduced that the reduction in density values with rising foaming temperatures is due to the simultaneous enlargement of the mean pore size linked to the elevated temperatures. This connection results in decreased material density due to the larger empty spaces within the foamed structure. Moreover, the data suggests that with prolonged processing time, the pore size remains relatively consistent, while the wall thickness of the material increases. The increase in wall thickness can contribute to higher density because of the greater amount of material within a specified volume.

In comparison, density values obtained in a previous work of ours [37] for sample processed in the same temperature condition, but using reagent-grade MnO_2 instead of exhausted battery cathodes, were lower.

3.5. Porosity

Considering an average density of soda-lime glass of 2500 kg m^{-3}, as experimentally evaluated (values in the range of 2400–2800 kg m^{-3} are reported in literature [56]), we can assume a porosity (as volumetric void fraction) between 0.87 (for heavier samples) to 0.89 (for lighter samples). Similar porosity values, determined as the complementary of the solid volume fraction calculated after μ-CT analysis, are reported in Table 2, alongside the thickness of the cell walls, the primary and secondary pore sizes. Fig. 11 depicts the relationship between primary and secondary pore sizes and glass foam density. The cell wall thickness is nearly identical in all samples (58–60 μm). Samples fabricated at higher temperatures exhibit larger primary pores, resulting in lower density, as illustrated in Fig. 11. Increasing the foaming time also leads to larger pores, although this effect is less pronounced than that achieved by increasing the temperature. The secondary pore size and porosity do not appear to be influenced by the processing temperature or time.

During the sintering process, achieving a soft state in the mixture is crucial for gas to form pores. For an effective foaming process, it is essential for the softening range of the glass to align with the highest activity of the expanding agent. Once the mixture reaches the peak sintering temperature, it should be held for a specific duration to promote pore growth and stabilize the microstructure. As the pores expand, the porosity of the glass foam increases, while the bulk density decreases. The optimal temperature and holding time depend on the composition of the mixture and the desired properties. As discussed in our previous work [37], higher temperatures are sometimes necessary to lower viscosities. However, such conditions can lead to the rapid formation and coalescence of gas bubbles, resulting in foam collapse and an increase in sample density. Prolonged standing times can also cause pore collapse as gas bubbles escape from the matrix due to their low specific weight, high pressure, and the low viscosity of the glass.

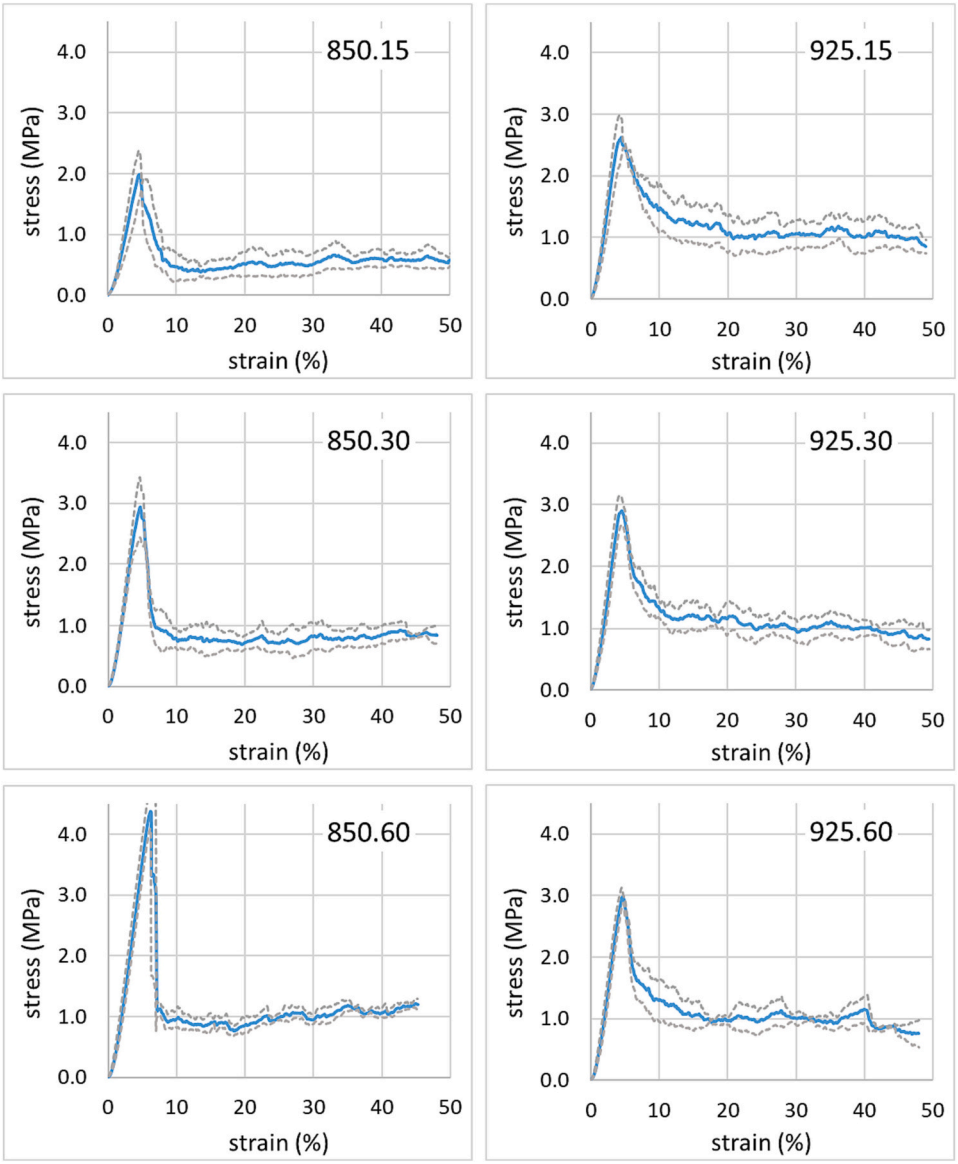

Fig. 13. Average compression stress-strain curves (in blue) for samples foamed at 850 and 925 °C, for different time (15, 30 and 60 min). Dashed curves represent standard deviation (5 compression tests for each sample type).

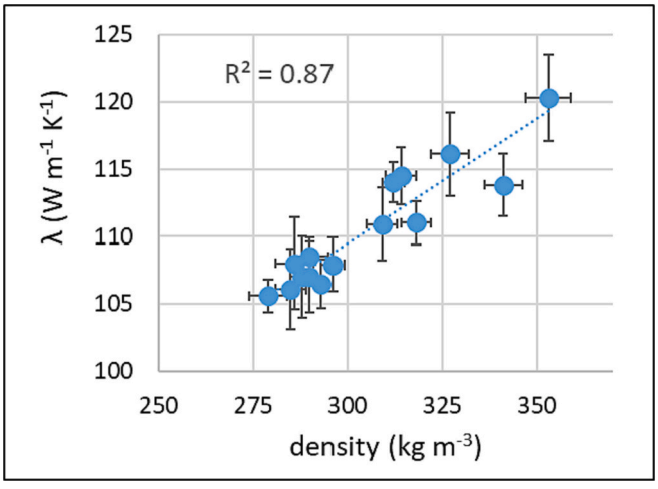

Fig. 14. Thermal conductivity λ as a function of sample density.

3.6. Mechanical properties

The average stress-strain curves obtained from the compression tests are depicted in Fig. 12 and Fig. 13. The compression modulus (E_C), strength (σ_C) and toughness (K) values determined after the compression tests are presented in Table 1.

The average values of E_C for samples processed at 850, 875 and 900 °C lie in the same range (from 58 to 61 MPa), while average value of E_C for samples processed at 925 °C and 950 °C is higher (≈71 and 83 MPa). Increasing foaming time from 15 to 60 min seem to increase the average values of E_C (73–80 MPa).

The average values of σ_C lie in the same range (2.7–2.8 MPa) for the samples foamed for 15 min at 875, 900 and 925 °C. Average value of σ_C (1.9 MPa) for samples sintered at 850 °C for 15 min is lower, while is higher (3.0 MPa) for sample processed at 950 °C. After increasing the foaming time to 30 and 60 min, the compression strength rises notably for samples processed at 850 °C (σ_C up to 4.6 MPa), while remain in the range of 3.0 MPa for samples processed at 925 °C.

Additionally, it can be observed that the energy absorbed before failure (proportional to the area beneath the stress-strain curve) is also

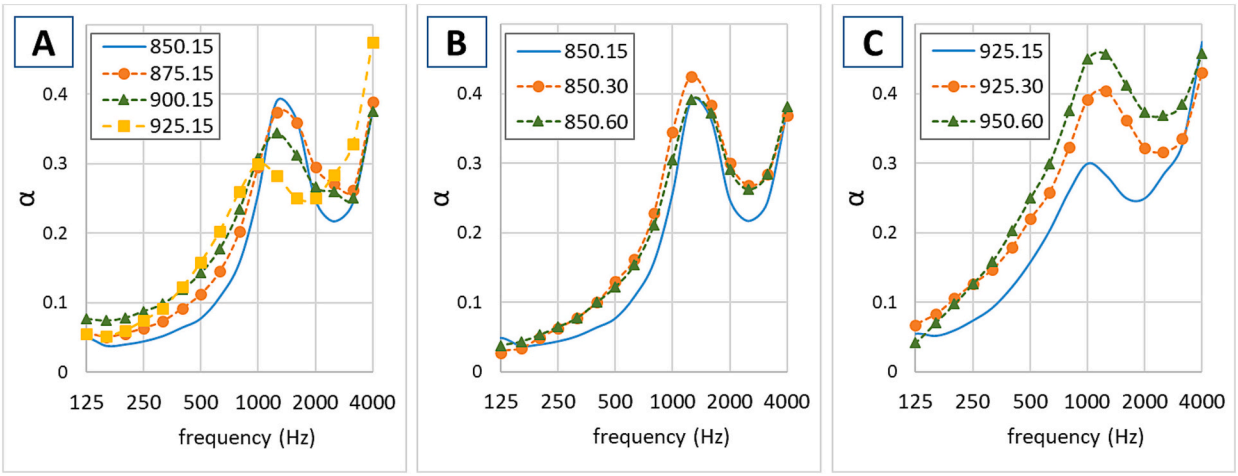

Fig. 15. Sound absorption curves of samples foamed for 15 min at different temperatures (A), samples foamed at 850 °C for different time (B) and samples foamed at 925 °C for different time (B).

higher for samples produced at 925 and 950 °C.

Interestingly, contrary to what was reported in our previous work, excluding samples foamed at 850 °C for 30 and 60 min (which exhibit high density and the best mechanical properties), the second highest strength properties are observed in samples with the lowest densities and the largest average pore sizes (specifically, samples foamed at 925 °C for 30 and 60 min). To explain this phenomenon, the influence of crystallinity should be taken into account (as discussed in paragraph 3.9). Upon conducting XRD analysis, it was found that samples sintered at higher temperatures exhibited the presence of devitrite crystals. These crystal phases appear to enhance the stiffness and strength of the foam. The increased crystalline content, associated with higher foaming temperatures, contributes to the improved mechanical properties despite the lower density.

Interestingly, none of the specimens demonstrate truly brittle breaking behavior (in fact, no specimen fails suddenly, as can be clearly observed from the curves). The overall toughness arises from the successive failure of cell structures, whose walls, made of glass, are individually brittle.

Overall, all samples exhibit mechanical properties superior to those of polymer foams (EPS and PU) [12,13,54,55] and they significantly outperform mineral-based insulation materials (glass wool and mineral wool) [57], making them particularly suitable for load-bearing applications. Overall, the mechanical properties of the samples obtained in this study are significantly superior compared to similar samples obtained using reagent-grade MnO_2 as a foaming agent. This suggests a lower effectiveness of the mix of Mn oxides derived from spent battery cathodes as an expansive agent. This is also consistent with the higher density observed in the samples obtained in this study with respect to that of samples fabricated using reagent-grade MnO_2.

3.7. Thermal insulation properties

The thermal conductivity (λ, reported in Table 1) ranges from 107 to 116 mW m^{-1} K^{-1}. It appear to be related to the density of the samples, with heavier ones showing higher conductivity values, as shown in Fig. 14. The λ values of the samples obtained using reagent-grade MnO_2 as a foaming agent are notably lower, in line with their lower densities.

In comparison, rock wool, glass wool, EPS, or PU foam outperform the samples, as their λ values range from 20 to 30 mW m^{-1} K^{-1} [7,12,13,54,55]. Thermal conductivity is affected by density but also by porosity type, with closed-cell structure favoring the thermal insulation. The majority of thermal conduction occurs in the solid phase, which is related to the sample density and contributes the most to the overall thermal conductivity. In an open-cell structure, conduction in the gas phase is more significant due to the different gas composition (air instead of CO_2) and the possibility of convective heat transfer [58,59].

3.8. Acoustic properties

The average sound absorption coefficient curves as a function of sound frequency are presented in Fig. 15, while the corresponding noise reduction coefficient (NRC) values are summarized in Table 1. The NRC values, representing the average α values across the 125–4000 Hz range, fall within a similar range of 0.2–0.3. These values are in line with those of commercially available sound-absorbing materials such as rigid polymeric foams or mineral wool [54,55]. Although no clear trend can be established, it can be noticed that the samples foamed for 15 min at lower temperatures (850 °C and 875 °C) have a higher α value, and this peak is shifted at higher frequencies. Increasing the foaming time lead to an improvement in the acoustic performances, particularly for samples foamed at 925 °C. The observed acoustic performance can be attributed to both density and porosity type, with open porosity offering superior acoustic insulation properties.

3.9. Crystallinity

The XRD analysis of the foamed samples (Fig. 16) revealed that the samples sintered for 15 min at 850 °C exhibited an amorphous structure. However, samples sintered at 875 °C, 900 °C, 925 °C, and 950 °C exhibited distinct diffraction peaks at approximately $2\theta \approx 27°$ and $2\theta \approx 30°$, indicating the presence of a crystalline phase identified as devitrite ($Na_2Ca_3Si_6O_6$) [60]. The crystalline content increased with higher foaming temperature and time. As shown in Fig. 16, also the foaming time influences the crystalline content. This higher crystalline content correlates with improved mechanical properties of samples foamed at 875, 900, 925 and 950 °C, and samples foamed at 850 °C for 60 min. The enhanced mechanical performance of the samples with higher crystalline content can be attributed to the reinforcing effect of the crystalline phase. Crystalline structures provide additional strength and rigidity to the material, resulting in higher modulus and strength values. Moreover, materials with similar porosity and density demonstrate increased rigidity and strength in the presence of higher crystallinity. On the other hand, the samples sintered at 850 °C for 15 min exhibit an amorphous structure, which is associated with relatively lower mechanical properties. The absence of a crystalline phase in these samples leads to reduced stiffness and lower strength, resulting in decreased mechanical performance. Therefore, it can be concluded that the presence of crystallinity, specifically the devitrite phase, positively influences the mechanical properties of the foamed samples.

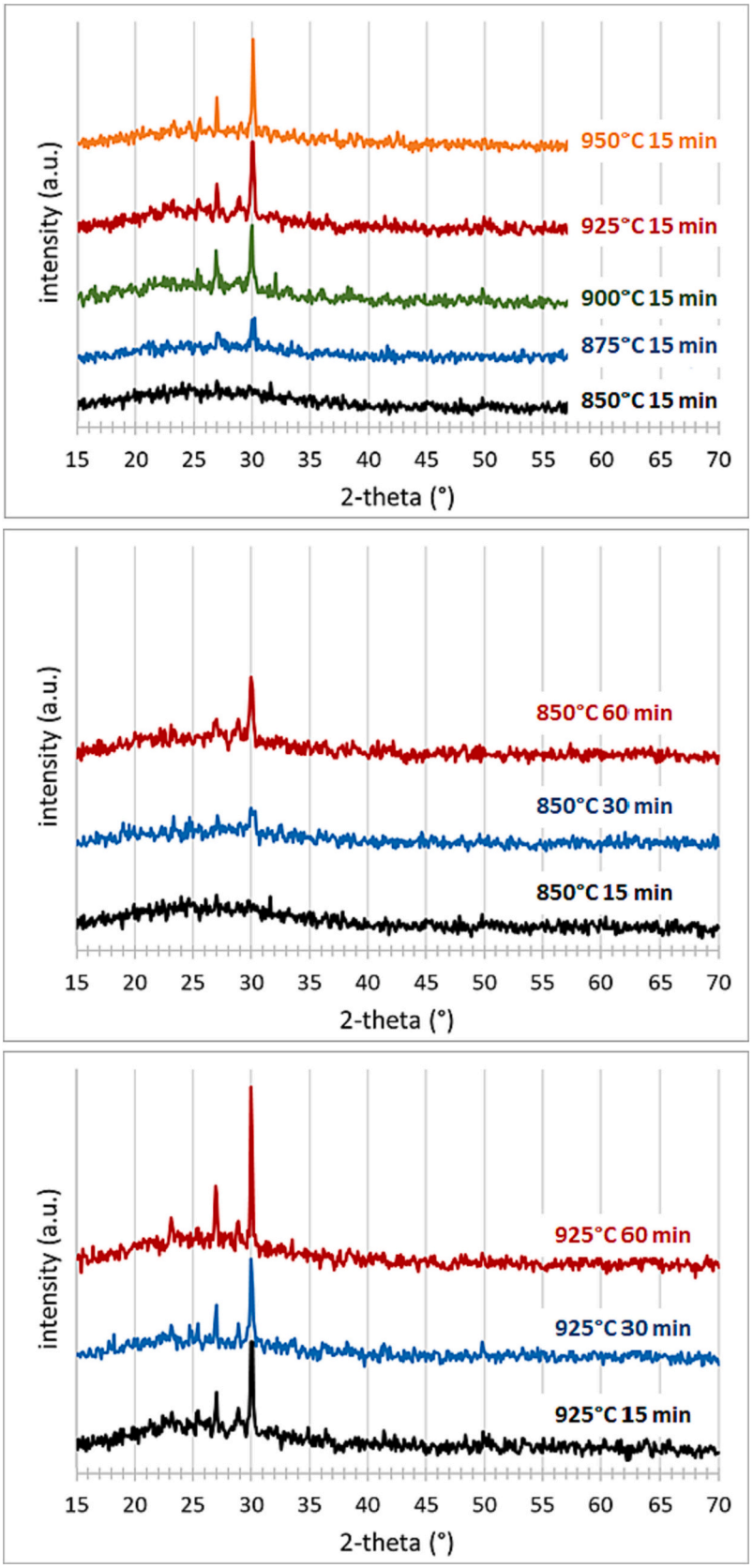

Fig. 16. XRD diffractograms of expanded glass processed at different temperatures and time. The identified crystalline phase is devitrite.

4. Conclusions

The results demonstrate the feasibility of producing glass foams using a mixture consisting of 97% *w*/w glass waste, 3% w/w spent alkaline battery cathodes, sintered at temperature ranging from 850 and 950 °C. These glass foams exhibit densities between 290 and 350 kg m^{-3}, porosities ranging from 88% to 90%, thermal conductivities between 105 and 120 mW m^{-1} K^{-1}, noise reducing factors of 0.2–0.3, and compressive strengths between 1.9 and 4.6 MPa. These materials offer an appealing combination of low weight, thermal/acoustic insulation and mechanical strength. While their insulation performance may not be exceptional compared to other materials like polymeric foams, they present a competitive alternative in load-bearing applications where stiffness, mechanical strength, chemical inertia, non-flammability, and high temperature resistance are crucial.

Despite the lower insulation performance of glass foam produced from glass waste and spent alkaline battery cathodes compared to those produced from commercially sourced Mn oxide, the utilization of waste materials offers compelling advantages for scientific research and sustainable materials development. In future manufacturing processes, the ability to reduce energy consumption, raw material usage, and CO_2 emissions will be of strategic importance and significant value. The production method employed in this study, which utilizes secondary raw materials, reduces energy requirements compared to the extraction, transportation, and processing of primary raw materials, leading to clear environmental benefits and improved environmental indices. Taking into account the substantial volumes of glass waste and alkaline batteries generated in the EU every year, the proposed method holds also significant potential for scalability and replicability, contributing to waste reduction and transformation into value-added products, aligning with circular economy principles.

Looking ahead, it will be worth considering the use of the entire battery, including both the anode and cathode. This approach has the potential to simplify the recycling process and maximize the recovery of all battery components. However, further research and experimentation are needed to assess the feasibility and effectiveness of this approach.

Declaration of Competing Interest

The authors declare that they have no known competing financial interests, personal relationships, intellectual property or other activities that could have appeared to influence the work reported in this paper.

Data availability

Data will be made available on request.

Appendix A. Supplementary data

Supplementary data to this article can be found online at https://doi.org/10.1016/j.susmat.2023.e00767.

References

[1] European Commission, EU 2030 Climate target plan. https://eur-lex.europa.eu/legal-content/EN/TXT/HTML/?uri=CELEX:52020DC0562, 2020 (accessed May 25, 2023).

[2] European Commission, REPowerEU Plan. https://eur-lex.europa.eu/legal-content/EN/TXT/HTML/?uri=CELEX:52022DC0230, 2022 (accessed May 25, 2023).

[3] US Environmental Protection Agency, EPA Sustainability Report and Implementation Plan 2020. https://www.epa.gov/sites/default/files/2020-10/documents/srip_fy20_508.pdf, 2020.

[4] US Dept. of Energy, Building Energy Data Book. https://openei.org/doe-opendata/dataset/6aaf0248-bc4e-4a33-9735-2babe4aef2a5/resource/3edf59d2-32be-458b-bd4c-796b3e14bc65/download/2011bedb.pdf, 2012.

[5] UN Environ. Program, Sustainable Buildings and Climate Initiative. https://www.unenvironment.org/explore-topics/resource-efficiency/what-we-do/cities/sustainable-buildings, 2013.

[6] European Commission, Energy Efficiency in Buildings. https://ec.europa.eu/info/news/focus-energy-efficiency-buildings-2020-lut-17, 2020.

[7] S. Schiavoni, F. D'Alessandro, F. Bianchi, F. Asdrubali, Insulation materials for the building sector: a review and comparative analysis, Renew. Sust. Energ. Rev. 62 (2016) 988–1011, https://doi.org/10.1016/j.rser.2016.05.045.

[8] L.F. Cabeza, A. Castell, M. Medrano, I. Martorell, G. Pérez, I. Fernández, Experimental study on the performance of insulation materials in Mediterranean construction, Energ. Build. 42 (2010) 630–636, https://doi.org/10.1016/j.enbuild.2009.10.033.

[9] D. Densley Tingley, A. Hathway, B. Davison, An environmental impact comparison of external wall insulation types, Build. Environ. 85 (2015) 182–189, https://doi.org/10.1016/j.buildenv.2014.11.021.

[10] A.C. Schmidt, A comparative life cycle assessment of building insulation products made of stone wool, paper wool and flax - Part 2, 2004, p. 8.

[11] F. Asdrubali, F. D'Alessandro, S. Schiavoni, A review of unconventional sustainable building insulation materials, Sustain. Mater. Technol. 4 (2015) 1–17, https://doi.org/10.1016/j.susmat.2015.05.002.

[12] B. Abu-Jdayil, A.-H. Mourad, W. Hittini, M. Hassan, S. Hameedi, Traditional, state-of-the-art and renewable thermal building insulation materials: an overview, Constr. Build. Mater. 214 (2019) 709–735, https://doi.org/10.1016/j.conbuildmat.2019.04.102.

[13] W. Villasmil, L.J. Fischer, J. Worlitschek, A review and evaluation of thermal insulation materials and methods for thermal energy storage systems, Renew. Sust. Energ. Rev. 103 (2019) 71–84, https://doi.org/10.1016/j.rser.2018.12.040.

[14] H. Gao, H. Liu, L. Liao, L. Mei, F. Zhang, L. Zhang, S. Li, G. Lv, A bifunctional hierarchical porous kaolinite geopolymer with good performance in thermal and sound insulation, Constr. Build. Mater. 251 (2020), 118888, https://doi.org/10.1016/j.conbuildmat.2020.118888.

[15] C. Ingrao, A. Lo Giudice, C. Tricase, R. Rana, C. Mbohwa, V. Siracusa, Recycled-PET fibre based panels for building thermal insulation: environmental impact and improvement potential assessment for a greener production, Sci. Total Environ. 493 (2014) 914–929, https://doi.org/10.1016/j.scitotenv.2014.06.022.

[16] A. Patnaik, M. Mvubu, S. Muniyasamy, A. Botha, R.D. Anandjiwala, Thermal and sound insulation materials from waste wool and recycled polyester fibers and their biodegradation studies, Energ. Build. 92 (2015) 161–169, https://doi.org/10.1016/j.enbuild.2015.01.056.

[17] H. Binici, M. Eken, M. Dolaz, O. Aksogan, M. Kara, An environmentally friendly thermal insulation material from sunflower stalk, textile waste and stubble fibres, Constr. Build. Mater. 51 (2014) 24–33, https://doi.org/10.1016/j.conbuildmat.2013.10.038.

[18] F. Intini, S. Kühtz, Recycling in buildings: an LCA case study of a thermal insulation panel made of polyester fiber, recycled from post-consumer PET bottles, Int. J. Life Cycle Assess. 16 (2011) 306–315, https://doi.org/10.1007/s11367-011-0267-9.

[19] R.K. Chinnam, A.A. Francis, J. Will, E. Bernardo, A.R. Boccaccini, Review. Functional glasses and glass-ceramics derived from iron rich waste and combination of industrial residues, J. Non-Cryst. Solids 365 (2013) 63–74, https://doi.org/10.1016/j.jnoncrysol.2012.12.006.

[20] F. Andreola, L. Barbieri, I. Lancellotti, C. Leonelli, T. Manfredini, Recycling of industrial wastes in ceramic manufacturing: state of art and glass case studies, Ceram. Int. 42 (2016) 13333–13338, https://doi.org/10.1016/j.ceramint.2016.05.205.

[21] G.A. Blengini, M. Busto, M. Fantoni, D. Fino, Eco-efficient waste glass recycling: integrated waste management and green product development through LCA, Waste Manag. 32 (2012) 1000–1008, https://doi.org/10.1016/j.wasman.2011.10.018.

[22] L. Cozzarini, L. Marsich, A. Ferluga, C. Schmid, Life cycle analysis of a novel thermal insulator obtained from recycled glass waste, Dev. Built Environ. 3 (2020), 100014, https://doi.org/10.1016/j.dibe.2020.100014.

[23] E. Bernardo, R. Cedro, M. Florean, S. Hreglich, Reutilization and stabilization of wastes by the production of glass foams, Ceram. Int. 33 (2007) 963–968, https://doi.org/10.1016/j.ceramint.2006.02.010.

[24] H.R. Fernandes, D.D. Ferreira, F. Andreola, I. Lancellotti, L. Barbieri, J.M. F. Ferreira, Environmental friendly management of CRT glass by foaming with waste egg shells, calcite or dolomite, Ceram. Int. 40 (2014) 13371–13379, https://doi.org/10.1016/j.ceramint.2014.05.053.

[25] G. Bayer, Foaming of borosilicate glasses by chemical reactions in the temperature range 950–1150°C, J. Non-Cryst. Solids 38–39 (1980) 855–860, https://doi.org/10.1016/0022-3093(80)90544-X.

[26] J. König, R.R. Petersen, Y. Yue, Influence of the glass–calcium carbonate mixture's characteristics on the foaming process and the properties of the foam glass, J. Eur. Ceram. Soc. 34 (2014) 1591–1598, https://doi.org/10.1016/j.jeurceramsoc.2013.12.020.

[27] A. Mazzi, M. Sciarrone, E. Bernardo, Environmental performance of glass foam as insulation material from waste glass with the alkali activation process, Heliyon. 9 (2023), e19001, https://doi.org/10.1016/j.heliyon.2023.e19001.

[28] J. König, R.R. Petersen, Y. Yue, Influence of the glass particle size on the foaming process and physical characteristics of foam glasses, J. Non-Cryst. Solids 447 (2016) 190–197, https://doi.org/10.1016/j.jnoncrysol.2016.05.021.

[29] J. König, R.R. Petersen, Y. Yue, D. Suvorov, Gas-releasing reactions in foam-glass formation using carbon and MnxOy as the foaming agents, Ceram. Int. 43 (2017) 4638–4646, https://doi.org/10.1016/j.ceramint.2016.12.133.

[30] J. König, R.R. Petersen, N. Iversen, Y. Yue, Suppressing the effect of cullet composition on the formation and properties of foamed glass, Ceram. Int. 44 (2018) 11143–11150, https://doi.org/10.1016/j.ceramint.2018.03.130.

[31] C. Mugoni, M. Montorsi, C. Siligardi, F. Andreola, I. Lancellotti, E. Bernardo, L. Barbieri, Design of glass foams with low environmental impact, Ceram. Int. 41 (2015) 3400–3408, https://doi.org/10.1016/j.ceramint.2014.10.127.

[32] J. König, R.R. Petersen, Y. Yue, Fabrication of highly insulating foam glass made from CRT panel glass, Ceram. Int. 41 (2015) 9793–9800, https://doi.org/10.1016/j.ceramint.2015.04.051.
[33] R.R. Petersen, J. König, Y. Yue, The mechanism of foaming and thermal conductivity of glasses foamed with MnO2, J. Non-Cryst. Solids 425 (2015) 74–82, https://doi.org/10.1016/j.jnoncrysol.2015.05.030.
[34] J. Yuwei Chi, B. Xu Lin, Effects of Fe2O3 on the properties of glass foams prepared by iron-containing solid waste, Glas. Phys. Chem. 45 (2019) 104–110, https://doi.org/10.1134/S1087659619020056.
[35] I. Avramov, C. Rüssel, R. Keding, Effect of chemical composition on viscosity of oxide glasses, J. Non-Cryst. Solids 324 (2003) 29–35, https://doi.org/10.1016/S0022-3093(03)00230-8.
[36] E.R. Stobbe, B.A. de Boer, J.W. Geus, The reduction and oxidation behaviour of manganese oxides, Catal. Today 47 (1999) 161–167, https://doi.org/10.1016/S0920-5861(98)00296-X.
[37] L. Cozzarini, L. De Lorenzi, N. Barago, O. Sbaizero, P. Bevilacqua, Expanded glass for thermal and acoustic insulation from recycled post-consumer glass and textile industry process waste, Materials. 16 (2023) 1721, https://doi.org/10.3390/ma16041721.
[38] Eurostat, Sales and collection of portable batteries and accumulators, 2023. https://ec.europa.eu/eurostat/databrowser/view/ENV_WASPB/default/table (accessed June 14, 2023).
[39] European Portable Battery Association, Primary and Rechargeable Batteries - Product Information. https://www.epbaeurope.net/assets/resources/EPBA_Product-Information_10112015.pdf, 2020 (accessed June 14, 2023).
[40] Panasonic, Alkaline Batteries - Technical handbook for professionals, 2020. https://mediap.industry.panasonic.eu/assets/custom-upload/Energy%20&%20Building/Batteries/Primary%20Batteries/Zinc%20Carbon%20and%20Alkaline%20Batteries/Panasonic%20Alkaline%20Batteries%20for%20Professionals%20Handbook.pdf (accessed June 14, 2023).
[41] M.F. Almeida, S.M. Xará, J. Delgado, C.A. Costa, Characterization of spent AA household alkaline batteries, Waste Manag. 26 (2006) 466–476, https://doi.org/10.1016/j.wasman.2005.04.005.
[42] Eurostat, Generation of waste by waste category, 2023. https://ec.europa.eu/eurostat/databrowser/view/ENV_WASGEN/default/table (accessed June 14, 2023).
[43] Eurostat, Packaging waste by waste management operations, 2023. https://ec.europa.eu/eurostat/databrowser/view/ENV_WASPAC_custom_6551229/default/table (accessed June 14, 2023).
[44] Yu.A. Spiridonov, L.A. Orlova, Problems of foam glass production, Glas. Ceram. 60 (2003) 313–314, https://doi.org/10.1023/B:GLAC.0000008234.79970.2c.
[45] Gabriella Dias, Sabrina Arcaro, Francielly Cesconeto, Bianca Maia, Fabiano Raupp-Pereira, Antonio Pedro Novaes De Oliveira, Production and characterization of glass foams for thermal insulation, Chem. Eng. Trans. 43 (2015) 1777–1782, https://doi.org/10.3303/CET1543297.
[46] ASTM International, ASTM C165–07 - Standard Test Method for Measuring Compressive Properties of Thermal Insulations. https://www.astm.org/c0165-07r17.html, 2007.
[47] International Organization for Standardization, Acoustics — Determination of sound absorption coefficient and impedance in impedance tubes — Part 2, 1998. https://www.iso.org/cms/render/live/en/sites/isoorg/contents/data/standard/02/28/22851.html (accessed September 1, 2022).
[48] ASTM International, ASTM C518 - Standard Test Method for Steady-State Thermal Transmission Properties by Means of the Heat Flow Meter Apparatus. https://www.astm.org/c0518-21.html, 2021 (accessed September 1, 2022).
[49] A.S. Llaudis, M.J.O. Tari, F.J.G. Ten, E. Bernardo, P. Colombo, Foaming of flat glass cullet using Si3N4 and MnO2 powders, Ceram. Int. 35 (2009) 1953–1959, https://doi.org/10.1016/j.ceramint.2008.10.022.
[50] E. Bernardo, G. Scarinci, P. Bertuzzi, P. Ercole, L. Ramon, Recycling of waste glasses into partially crystallized glass foams, J. Porous. Mater. 17 (2010) 359–365, https://doi.org/10.1007/s10934-009-9286-3.
[51] C. Lucktong, P. Hrma, Oxygen evolution during MnO-Mn3O4 dissolution in a borosilicate melt, J. Am. Ceram. Soc. 71 (1988) 323–328, https://doi.org/10.1111/j.1151-2916.1988.tb05048.x.
[52] R.R. Petersen, J. König, Y. Yue, The viscosity window of the silicate glass foam production, J. Non-Cryst. Solids 456 (2017) 49–54, https://doi.org/10.1016/j.jnoncrysol.2016.10.041.
[53] C. Venturelli, Heating microscopy and its applications, Micros. Today 19 (2011) 20–25, https://doi.org/10.1017/S1551929510001185.
[54] ASTM International, ASTM C578–18 - Standard, Specification for Rigid, Cellular Polystyrene Thermal Insulation. https://www.astm.org/c0578-18.html, 2018.
[55] ASTM International, ASTM C1029–20 - Standard Specification for Spray-Applied Rigid Cellular Polyurethane Thermal Insulation. https://www.astm.org/c1029-20.html, 2020.
[56] T.P. Seward III, T. Vascott, High Temperature Glass Melt Property Database for Process Modeling | Wiley, Wiley, 2005.
[57] A. Buska, R. Mačiulaitis, The compressive strength properties of mineral wool slabs: influence of structure anisotropy and methodical factors, J. Civ. Eng. Manag. 13 (2007) 97–106, https://doi.org/10.1080/13923730.2007.9636425.
[58] J.P. Holman, Heat Transfer, 7th ed., McGraw-Hill Education, 2012.
[59] J. König, A. Lopez-Gil, P. Cimavilla-Roman, M.A. Rodriguez-Perez, R.R. Petersen, M.B. Østergaard, N. Iversen, Y. Yue, M. Spreitzer, Synthesis and properties of open- and closed-porous foamed glass with a low density, Constr. Build. Mater. 247 (2020), 118574, https://doi.org/10.1016/j.conbuildmat.2020.118574.
[60] V. Kahlenberg, D. Girtler, E. Arroyabe, R. Kaindl, D.M. Többens, Devitrite (Na2Ca3Si6O16)—structural, spectroscopic and computational investigations on a crystalline impurity phase in industrial soda-lime glasses, Mineral. Petrol. 100 (2010) 1–9, https://doi.org/10.1007/s00710-010-0116-8.